



## OPEN Novel bilayer 2D V<sub>2</sub>O<sub>5</sub> as a potential catalyst for fast photodegradation of organic dyes

P. R. Reshma<sup>✉</sup>, Arun K. Prasad & Sandip Dhara

Two-dimensional (2D) materials have recently drawn interest in various applications due to their superior electronic properties, high specific surface area, and surface activity. However, studies on the catalytic properties of the 2D counterpart of V<sub>2</sub>O<sub>5</sub> are scarce. In the present study, the catalytic properties of 2D V<sub>2</sub>O<sub>5</sub> vis-à-vis bulk V<sub>2</sub>O<sub>5</sub> for the degradation of methylene blue dye are discussed for the first time. The 2D V<sub>2</sub>O<sub>5</sub> catalyst was synthesized using a modified chemical exfoliation technique. A massive increase in the electrochemically active surface area of 2D V<sub>2</sub>O<sub>5</sub> by one order of magnitude greater than that of bulk V<sub>2</sub>O<sub>5</sub> was observed in this study. Simultaneously, ~ 7 times increase in the optical absorption coefficient of 2D V<sub>2</sub>O<sub>5</sub> significantly increases the number of photogenerated electrons involved in the catalytic performance. In addition, the surface activity of the 2D V<sub>2</sub>O<sub>5</sub> catalyst is enhanced by generating surface oxygen vacancy defects. In the current study, we have achieved ~ 99% degradation of 16 ppm dye using the 2D V<sub>2</sub>O<sub>5</sub> nanosheet catalysts under UV light exposure with a remarkable degradation rate constant of 2.31 min<sup>-1</sup>, which is an increase of the order of 10<sup>2</sup> from previous studies using V<sub>2</sub>O<sub>5</sub> nanostructures and nanocomposites as catalysts. Since the enhanced photocatalytic activity emerged from the surface and optical properties of the catalyst, the current study shows great promise for the future application of 2D V<sub>2</sub>O<sub>5</sub> in photo- and electrocatalysis.

Two-dimensional (2D) materials exhibit exotic physical, electrical, and optical properties that vary from their bulk counterparts. By altering the number of layers, the properties of 2D materials can be tailored. This distinctiveness provides opportunities for controlling the surface, optical, magnetic, and electrical properties of 2D materials for a range of applications. 2D materials are excellent choices for applications involving surface redox reactions, such as catalysis and gas sensing, because of their very high specific surface area and density of surface active states<sup>1–8</sup>. For instance, graphene exhibits a high specific surface area of ~ 2600 m<sup>2</sup>/g, whereas it is ~ 8 m<sup>2</sup>/g for natural graphite<sup>9</sup>. In addition to the high surface-to-volume ratio<sup>9</sup>, the presence of edge defects in 2D structures, which are responsible for stabilizing the structure, enhances the catalytic properties. For example, graphene with zig-zag edges shows good catalytic activity<sup>10</sup>. Theoretically, edge defect states strongly increase the electronic density of states at the edges compared to the plane of 2D materials<sup>11</sup>. In addition, the presence of dislocations, vacancy defects, impurities, and functional groups can significantly increase the density of surface active states and, consequently, the catalytic activity of the materials<sup>12</sup>. The impressive mechanical stability, generally shown by 2D materials, offers high stability and durability as catalysts and catalyst supports. Additionally, materials such as graphene, which has high electrical conductivity, have been applied in electrocatalysis.

The effluent from the textile industry contains organic dye molecules that are potentially harmful to human health and the ecosystem. Textile dyes are non-biodegradable and generally highly stable under light, heat, and oxidizer exposure<sup>13</sup>. Generally, catalyst-mediated redox reactions are cost-effective methods for the degradation of textile dyes<sup>14–16</sup>. Semiconducting metal oxides with bandgaps in the range of visible and UV light energies, such as V<sub>2</sub>O<sub>5</sub><sup>17</sup>, SnO<sub>2</sub><sup>18</sup>, ZnO<sup>19</sup>, ZrO<sub>2</sub><sup>20</sup>, and TiO<sub>2</sub><sup>21,22</sup>, are generally used as photocatalysts. As a transition metal, V possesses multiple oxidation states<sup>23</sup>, and the vanadium oxide surface can undergo reversible redox reactions<sup>24,25</sup>. This property makes V<sub>2</sub>O<sub>5</sub> a promising catalyst. In addition, V<sub>2</sub>O<sub>5</sub> nanostructures with various morphologies and heterostructures of V<sub>2</sub>O<sub>5</sub>/rGO, and V<sub>2</sub>O<sub>5</sub>/graphene also show good catalytic performance<sup>26–28</sup>. Under ambient conditions, V<sub>2</sub>O<sub>5</sub> crystallizes in its orthorhombic polymorph  $\alpha$ -V<sub>2</sub>O<sub>5</sub>, a layered van der Waals crystal<sup>29</sup>. The surface of the V<sub>2</sub>O<sub>5</sub> catalyst consists of three differently coordinated oxygen atoms: vanadyl (O<sub>1</sub>), bridge (O<sub>II</sub>), and chain (O<sub>III</sub>) oxygen (the number in the subscript indicative of the coordination number of the oxygen atom)<sup>29</sup>. The bridging oxygen connects the double V–O chains in the crystal structure along the *b*-axis. The VO<sub>4</sub> sites on

Materials Science Group, Indira Gandhi Centre for Atomic Research, A CI of Homi Bhabha National Institute, Kalpakkam 603102, Tamil Nadu, India. <sup>✉</sup>email: reshmapattaniparambil@gmail.com; akp@igcar.gov.in

the *ab*-plane  $V_2O_5$  surface are the active surface sites for catalysis<sup>30</sup>. The supported vanadium oxide catalysts on oxide surfaces also tend to show improved catalytic performance by controlling the specific activity of  $VO_4$  sites<sup>30</sup>.

Using 2D  $V_2O_5$ , one can significantly reduce the defect formation energy and increase the active surface area for the catalytic reaction, consequently improving the catalytic performance. However, the catalytic properties of the 2D counterpart of  $V_2O_5$  have not been reported before. The present study thoroughly examined the catalytic property of 2D  $V_2O_5$  for the degradation of organic dyes. The chemically exfoliated  $V_2O_5$  nanosheets were used as catalysts in the current study. The photocatalytic performance of 2D  $V_2O_5$  for the degradation of methylene blue (MB) dye was investigated and compared with that of bulk  $V_2O_5$ .

## Methods

### Synthesis and characterization of 2D $V_2O_5$ nanosheets

2D  $V_2O_5$  nanosheets were synthesized by a modified chemical exfoliation method by altering the concentration of bulk  $V_2O_5$  in formamide<sup>29</sup>. Previous reports have shown that  $V_2O_5$  intercalated with formamide molecules can provide a stable suspension of tiny flakes of  $V_2O_5$  in formamide medium<sup>29,31</sup>. For the synthesis, bulk  $V_2O_5$  powder (Merck, 99.99%) was dispersed in formamide (Merck, 99%) for 24 h. To separate the exfoliated nanosheets, the dispersion of formamide-intercalated  $V_2O_5$  was subjected to a 1 h ultrasonic treatment at room temperature. The resultant suspension was then coated on a quartz substrate by drop casting (for the photocatalysis study), followed by heating at 100 °C to completely remove the formamide molecules. Furthermore, the exfoliated nanosheets were annealed for three hours at 250 °C under a continuous flow of  $O_2$ <sup>29</sup>. The substrate was replaced with  $SiO_2/Si$  and high pure gold for AFM and Raman spectroscopic studies, respectively.

A multimode scanning probe microscope (INTEGRA, NT-MDT, Russia) was used to record the atomic force microscopy (AFM) topography and estimate the thickness of the exfoliated nanosheets coated on the  $SiO_2/Si$  substrate. Intermittent contact mode was used for imaging. Atomic-resolution STEM images were collected using probe aberration-corrected Thermo Fisher Scientific Themis Z ultrahigh-resolution TEM at an acceleration voltage of 300 kV. Oxygen vacancy defects in the sample were identified using X-ray photoelectron spectroscopy (XPS) (SPECS Surface Nano Analysis GmbH, Germany). A monochromatic Al  $K_\alpha$  X-ray source (1486.7 eV) was used for the XPS measurements. Ultraviolet-visible (UV–Vis) absorption spectroscopy (Avantes) was carried out in absorption mode to determine the band gap. UV–Vis absorption spectra of the bulk and 2D  $V_2O_5$  nanosheets were collected using a cuvette with a width of 1 cm and the same light source. Raman spectroscopy (InVia, Renishaw, UK) was carried out utilizing a 532 nm Nd:YAG solid-state laser as the excitation source in the backscattering geometry, an 1800 g/mm grating, and a thermoelectrically cooled charged coupled device as the detector.

### Estimation of specific surface area

The electrochemically active surface area (ECSA) of bulk and 2D  $V_2O_5$  were calculated and compared. The ECSA was estimated from the non-Faradic capacitive current associated with double layer charging using the scan rate dependence of cycle voltammograms (CV)<sup>32,33</sup>. The experimental setup consists of a three-electrode system with a Pt counter electrode and Ag/AgCl as the reference electrode. In the present study, for bulk  $V_2O_5$ , a 5 mM dispersion of bulk  $V_2O_5$  in propanol was taken. Around 630  $\mu$ L was dispersed on carbon paper with dimensions of 1.5 cm × 1.5 cm. The volume of the sample dispersion was chosen to ensure a conformal coating on the carbon paper. For 2D  $V_2O_5$ , 250  $\mu$ L of a 1 mM dispersion of exfoliated  $V_2O_5$  nanosheets (45  $\mu$ g of sample) in formamide was coated on a similar substrate. The CV of the samples with 1 M  $H_2SO_4$  electrolyte was recorded (using PGSTAT 302 N, Metrohm Autolab e.v.), and the peak current,  $I_c$ , was taken from the non-Faradic region.

### Photocatalytic study

The degradation of MB ( $C_{16}H_{18}ClN_3S$  (Merck India)) dye was examined to understand the photocatalytic properties of the bulk material and 2D  $V_2O_5$ . The  $V_2O_5$  catalyst mixed with the dye was subjected to UV-C (254 nm, 9 W, PL-S, PHILIPS, Poland). The intensity of the light source was measured using a Lutron UV light meter (Taiwan) at a distance of 3 cm from the light source, and the intensity was 2.21 mW/cm<sup>2</sup>. An aqueous solution of dye and bulk  $V_2O_5$  (concentration 0.18 mg/mL) was prepared in the dark and maintained at adsorption–desorption equilibrium. For 2D  $V_2O_5$ , 5 mL of 2D  $V_2O_5$  dispersion (around 0.9 mg) was deposited on a quartz substrate and dipped into dye solution<sup>32</sup>. To achieve adsorption–desorption equilibrium, the sample was kept in the dark. The amount of 2D  $V_2O_5$  sample was selected so that, for 5 mL of stock solution, the catalyst amount maintained the same as that for the bulk  $V_2O_5$  catalyst. Light source was then exposed upon the dye solution containing the catalyst for various durations. Five milliliters of the irradiated solution was then subjected to UV–Vis spectrometry. By monitoring the MB dye absorption peak at 664 nm, the degradation of MB dye was studied. For the quantitative study, the UV–Vis absorption spectra of the solutions were periodically recorded.

## Results and discussion

### Estimation of nanosheet thickness and atomic resolution STEM studies

AFM studies were carried out on the exfoliated  $V_2O_5$  sample to determine the thickness. Figure 1a shows the AFM image of evenly distributed nanosheets on a  $Si/SiO_2$  substrate. The exfoliated layers in the ensemble have lateral dimensions between 100 and 300 nm, as observed from the FESEM image (Fig. S1). The observed step height has a standard deviation of 0.1 nm. The theoretical thicknesses of the monolayer, bilayer and trilayer  $V_2O_5$  nanosheets are ~ 0.43, 0.87 and 1.3 nm, respectively<sup>29</sup>. The experimentally observed thicknesses of the individual layers of 2D  $V_2O_5$  nanosheets are in the range of 1.0–1.5 nm, as shown in the height profile (Fig. 1a). The numerical distribution of the nanosheet thicknesses shown in Fig. 1b indicates that the quantity of bilayer thin nanosheets in the sample is substantially greater. To verify the atomic structure and chemical composition,

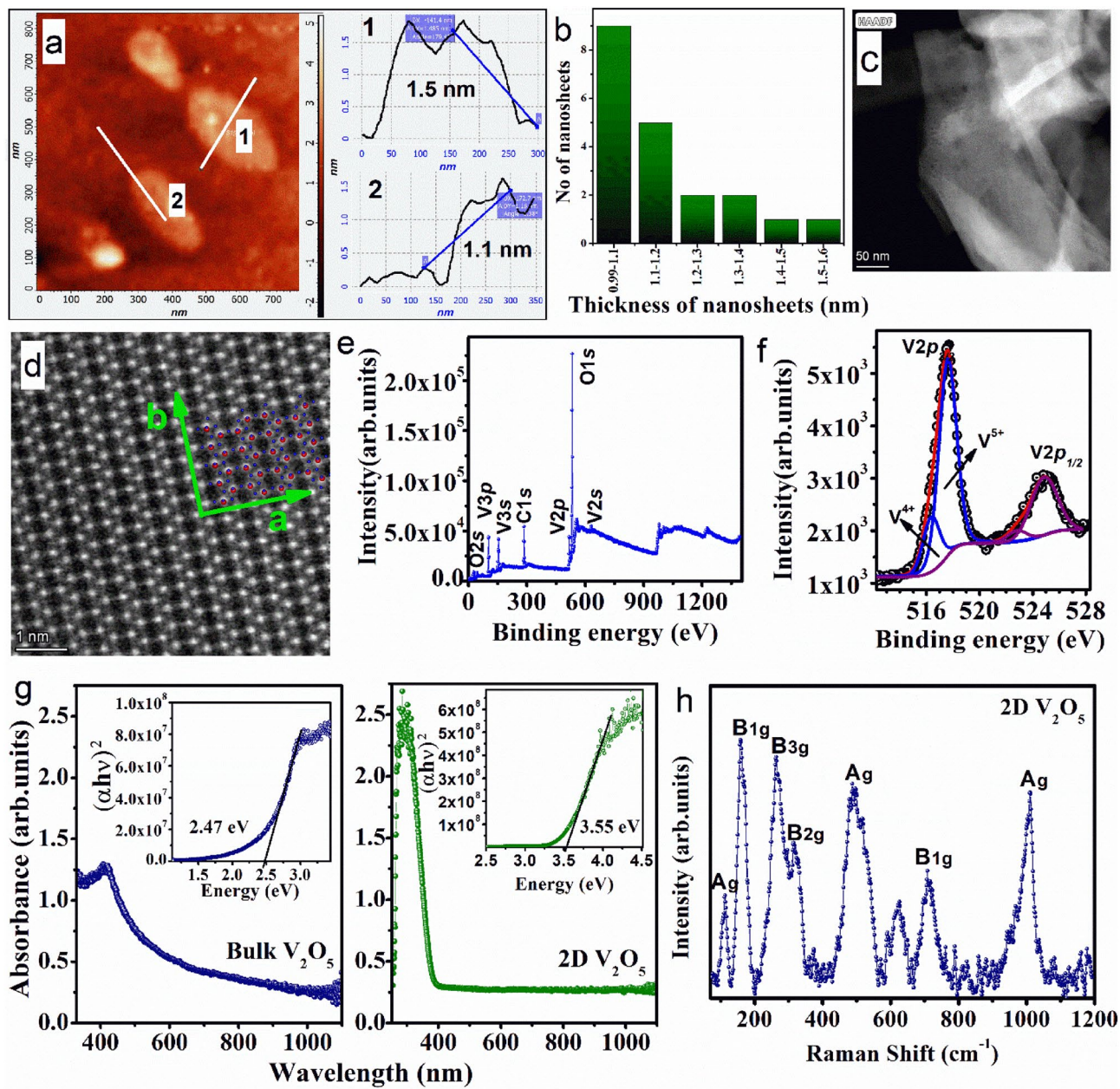


**Figure 1.** (a) AFM topography and height profile of exfoliated nanosheets. (b) Distribution of the thickness of 2D V<sub>2</sub>O<sub>5</sub> nanosheets. (c) STEM image and (d) atomic resolution annular dark field (ADF)-STEM image of 2D V<sub>2</sub>O<sub>5</sub> nanosheets. (e) XPS survey spectrum of 2D V<sub>2</sub>O<sub>5</sub> and (f) the core-level spectrum corresponding to the binding energies of V2p<sub>3/2</sub> for the V<sup>5+</sup> and V<sup>4+</sup> states of V atoms in 2D V<sub>2</sub>O<sub>5</sub> nanosheets. (g) UV–Vis absorption spectra of bulk and 2D V<sub>2</sub>O<sub>5</sub>. The Tauc plot for understanding the optical band gap is given in the corresponding insets. (h) Raman spectrum of the 2D V<sub>2</sub>O<sub>5</sub> nanosheets.

an atomic resolution scanning transmission electron microscopy (STEM) image of the exfoliated nanosheets was obtained. Figure 1c and d show dark field (DF) STEM image and atomic resolution annular dark field (ADF)-STEM image of 2D nanosheets. The nanosheets in the DF-STEM image shown in Fig. 1c are folded, which is commonly observed in unsupported 2D structures<sup>34</sup>. The atomic resolution ADF image, displayed in Fig. 1d, is collected from the flat area of the individual nanosheets and demonstrates the arrangement of the VO<sub>5</sub> square pyramidal structure in  $\alpha$ -V<sub>2</sub>O<sub>5</sub> along the (001) plane. The 2D layer is generated by joining the 1D chain of VO<sub>5</sub> pyramids along the *b*-axis with chain oxygen (O<sub>II</sub>) along the *a*-axis.

#### X-ray photoelectron spectroscopy studies

Figure 1e displays the XPS survey spectrum of 2D V<sub>2</sub>O<sub>5</sub>. The V<sub>2</sub>O<sub>5</sub> phase of the exfoliated nanosheets was further validated by the observation of peaks at 517.4 (V2p<sub>3/2</sub>), 524.8 (V2p<sub>1/2</sub>), and 530.1 (O1s) in the XPS survey spectrum<sup>35</sup>. The deconvoluted peaks in the core-level spectrum observed at 517.4 and 516.3 eV corresponded

to the binding energies of  $V2p_{3/2}$  for the  $V^{5+}$  and  $V^{4+}$  states, respectively (Fig. 1f). The peaks at 524.8 and 523.1 eV correspond to the binding energies of  $V2p_{1/2}$  for the  $V^{5+}$  and  $V^{4+}$  states, respectively<sup>36</sup>. The presence of the peaks corresponding to  $V^{4+}$  indicates the presence of oxygen vacancy sites in the samples<sup>29</sup>. The percentage of oxygen vacancy defects in 2D  $V_2O_5$  was ~17%, as determined by the area under the curve. The presence of these oxygen vacancy sites can potentially increase the surface activity and, consequently, the catalytic property of the sample.

### UV–Vis absorption studies for estimating the optical band gap

Bulk  $V_2O_5$  is a semiconductor with a bandgap of ~2.4 eV and a Fermi energy between the O 2p valence band and V 3d conduction band<sup>37</sup>. Within this gap, however, two localized split-off bands exist approximately 0.6 eV below the main V 3d band due to crystal field splitting<sup>37</sup>. The xy-derived levels of the conduction band are predicted to be at the lowest energies because they are not affected by vanadyl oxygen interactions. However, only two of the four xy-derived levels interact with the bridging oxygen and move up into the conduction band. Hence, the strong, indirect V–V interactions across the bridging oxygen are found to be the cause of the existence of split-off bands<sup>37</sup>. Figure 1g shows the UV–Vis absorption spectra and Tauc plots for estimating the band gap for bulk and 2D  $V_2O_5$ . A significant increase in the absorbance value from 0.22 to 1.58 was seen between bulk and bilayer  $V_2O_5$  (Fig. 1g). Additionally, there is a substantial increase in the optical absorbance for 2D and bulk  $V_2O_5$  with the same concentration of sample and intensity of incident light. This observation is possibly due to the pronounced excitonic effects in bilayer 2D  $V_2O_5$ , which is also observed in other 2D materials arising out of the reduced dielectric screening effect<sup>38,39</sup>. This increase in the optical absorbance of 2D  $V_2O_5$  indicates an exceptionally high number of photogenerated free charges, which can actively participate in the photocatalytic process. In addition, an absorption edge blueshift from bulk to bilayer 2D  $V_2O_5$  was observed, indicating electronic decoupling with decreasing layer thickness in the 2D nanosheets of  $V_2O_5$ <sup>29</sup>. The optical bandgap and  $E_g$  of bulk and 2D  $V_2O_5$  are experimentally calculated from Tauc's Plot to be 2.47 and 3.55 eV, respectively (Fig. 1g). These results are in agreement with our earlier report on the synthesis of 2D nanosheets of  $V_2O_5$ <sup>29</sup>.

### Raman spectroscopic analysis of bilayer 2D $V_2O_5$

The Raman spectrum of the 2D  $V_2O_5$  is given in Fig. 1h. The sample exhibited nine vibrational modes corresponding to 2D  $V_2O_5$ . The low-frequency vibrational modes  $A_{1g}$  and  $B_{1g}$  at 111 and 158 cm<sup>-1</sup>, respectively, are due to chain translation along the crystallographic *c*- and *a*-axes. V–O<sub>II</sub>–V bending vibration causes the  $B_{3g}$  mode at 262 cm<sup>-1</sup>. The deflection of V–O<sub>III</sub> and V–O<sub>III'</sub> along the *c* direction is responsible for the vibrational mode  $B_{2g}$  at 324 cm<sup>-1</sup>. The  $A_{1g}$  peak at 489 cm<sup>-1</sup> arises from the bending vibration of V–O<sub>II</sub>–V in the *c* direction. The vibration of V–O<sub>III'</sub> and V–O<sub>III</sub> along the *a*-axis is the origin of the vibrational mode  $B_{1g}$  at 713 cm<sup>-1</sup>. The highest frequency  $A_{1g}$  mode at 1010 cm<sup>-1</sup> corresponds to the stretching vibration of V–O<sub>I</sub> along the *c*-axis<sup>29</sup>. The peak at 620 cm<sup>-1</sup> in the Raman spectrum is expected to arise due to surface oxygen vacancies and consequent surface reduction<sup>29</sup>.

### Electrochemical surface area of bulk and 2D $V_2O_5$

The specific surface area of the 2D  $V_2O_5$  nanosheets was compared with that of bulk  $V_2O_5$  by calculating the ECSA. The ECSA of a sample is essentially estimated from the electrochemical double-layer capacitance. The measurement can be performed either from the non-Faradic capacitive current associated with double-layer charging from the scan rate dependence of CV or from the frequency-dependent impedance of the system using electrochemical impedance spectroscopy<sup>32,39</sup>. In the present study, the first method was adopted for the measurement of the ECSA. The faradic process will be absent in the potential window of, typically, 0.1 V around the open circuit voltage. The CV curves of the samples were recorded using 1 M  $H_2SO_4$  as the electrolyte. From the non-Faradic part, the peak current,  $I_C$ , is obtained. Thus, the ECSA may be determined using,

$$ECSA = \frac{C_{dl}}{C_s} \quad (1)$$

where  $C_s$  is the specific capacitance of an atomically smooth planar surface of the material per unit area under identical electrolyte conditions. For the 1 M  $H_2SO_4$  electrolyte, the  $C_s$  were found to be 0.035 mF/cm<sup>32,39,40</sup>. Figure 2a and b show CV diagrams of bulk and 2D  $V_2O_5$ , respectively. The values of the double layer capacitance ( $C_{dl}$ ) are 1.29 mF for bulk, as shown in Fig. 2c, and 3.32 mF for 2D  $V_2O_5$ , as shown in Fig. 2d. The corresponding ECSAs per 1 g of bulk and 2D  $V_2O_5$  were determined to be 6.5 and 211 m<sup>2</sup>/g, respectively (Fig. 2e). According to the literature, bulk  $V_2O_5$  has a shallow specific surface area < 10 m<sup>2</sup>/g<sup>31,32</sup>. Thus, the observed specific surface area of bulk  $V_2O_5$  is in agreement with the literature. This study revealed that, in comparison with the bulk equivalent, 2D nanosheets of  $V_2O_5$  exhibited an increase in specific surface area of approximately 32 times.

### Degradation of MB dye under UV irradiation

The photodegradation of MB dye was studied using bulk and 2D  $V_2O_5$  as catalysts. The UV–Vis absorption spectra of aqueous dye solutions collected at various UV light exposure times containing the bulk and 2D  $V_2O_5$  catalysts are displayed in Fig. 3a and b. The benzene ring and heteropoly aromatic bond of the MB dye molecule are broken upon exposure to UV light in the presence of the catalyst, which is apparent from the decrease in the strength of the absorption peak at 662 and 608 nm<sup>32,41</sup>. As a result, upon exposure to UV light in the presence of the catalyst, the dye molecules undergo degradation. The amount of catalyst was kept the same for all bulk and 2D  $V_2O_5$  samples for the same amount of dye solution. The photodegradation of MB dye under UV light exposure without any catalysts was also tested and is shown in Fig. S2 (Supplementary information). The degradation of MB dye using 2D and bulk  $V_2O_5$  catalysts was also studied under exposure to visible light, and

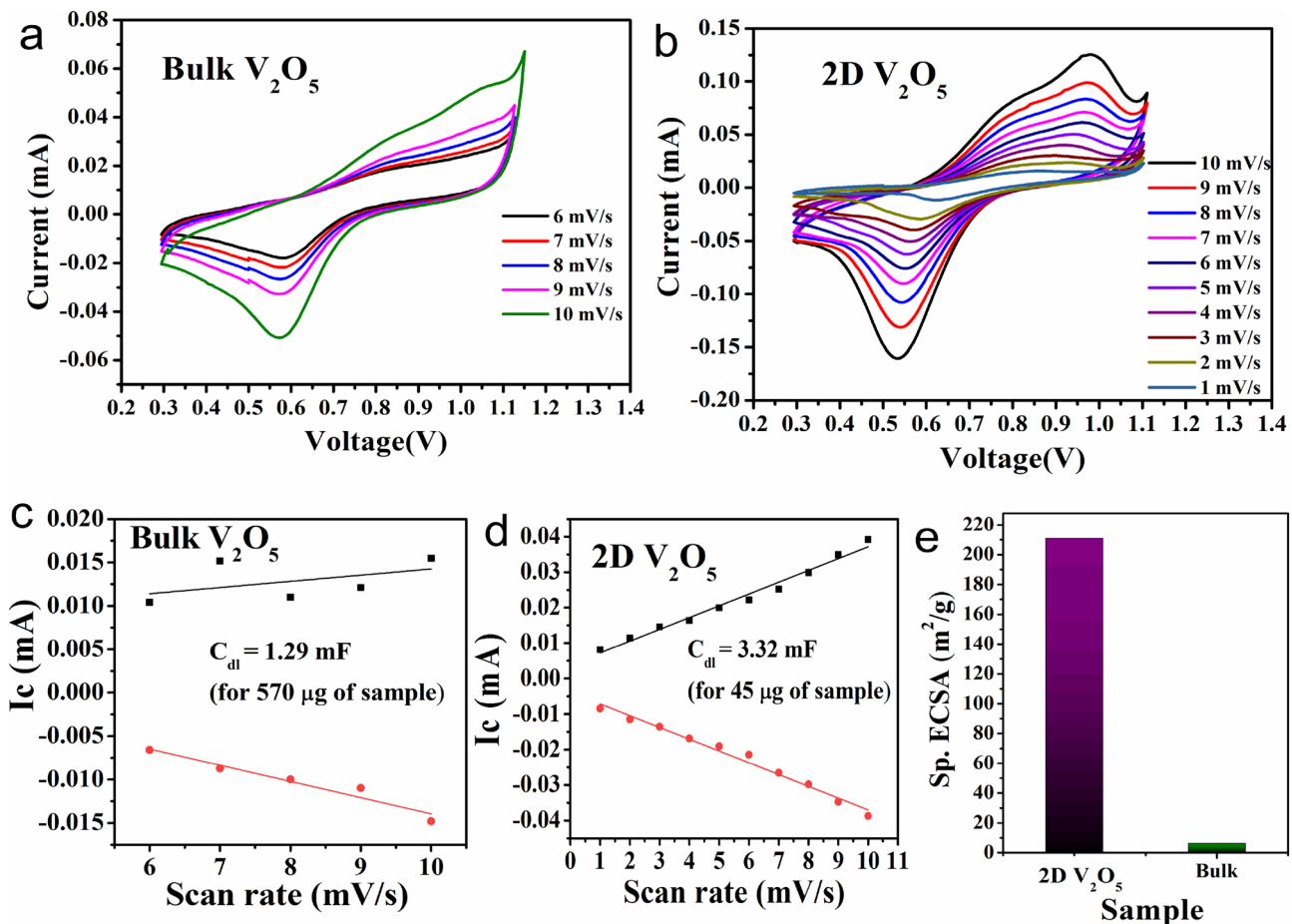


**Figure 2.** CV diagram of (a) bulk  $\text{V}_2\text{O}_5$  and (b) 2D  $\text{V}_2\text{O}_5$ . Peak current versus scan rate in the non-Faradic region for (c) bulk  $\text{V}_2\text{O}_5$  and (d) 2D  $\text{V}_2\text{O}_5$ . (e) ECSA for 1 g of bulk and 2D  $\text{V}_2\text{O}_5$ .

the results are shown in the supplementary information (Fig. S3). Only ~ 5% of the dye underwent degradation with a UV light exposure of 160 min. As shown in Fig. 3a and b, the bulk  $\text{V}_2\text{O}_5$  catalyst caused only minimal degradation of 7.7% after 35 min of UV exposure of the dye (16 ppm), whereas 2D  $\text{V}_2\text{O}_5$  catalyst resulted in the degradation of ~ 99% in just 3 min.

#### Estimation of the rate constant and efficiency of dye degradation

Generally, the degradation obeys pseudo-first-order kinetics<sup>32,41,42</sup>, and according to the observations, the degradation reaction fits well with the equation  $\ln \frac{C_0}{C_t} = kt$ , where  $C_0$  is the absorption at  $t=0$ , and  $C_t$  is the absorption after the time interval  $t$  of the irradiation (Fig. 3c). Based on Fig. 3c, the rate constants for dye degradation using the bulk and exfoliated  $\text{V}_2\text{O}_5$  catalysts were calculated. The 2D and bulk  $\text{V}_2\text{O}_5$  catalysts exhibit distinct rate constants for the degradation of MB dye:  $2.311 \text{ min}^{-1}$  and  $0.0023 \text{ min}^{-1}$ , respectively.

The percentage (%) of photocatalytic dye degradation efficiency was calculated using Eq. (2)<sup>43</sup>.

$$D(\%) = \frac{C_0 - C_t}{C_0} \times 100 \quad (2)$$

Figure 3d depicts the effect of light exposure duration on degradation efficiency. As discussed in the previous sections, the specific surface areas (ECSA) of the bulk and 2D  $\text{V}_2\text{O}_5$  are 6.5 and  $211 \text{ m}^2/\text{g}$ , respectively. As a result of this increase in the specific surface area, the photocatalytic performance of the 2D nanosheets substantially improved compared with that of the bulk  $\text{V}_2\text{O}_5$  catalyst. In addition, surface oxygen vacancies can act as active sites for redox reactions and enhance surface activity. A comparison of the reported literature with the present study (Table 1) also indicates the superior catalytic performance of 2D  $\text{V}_2\text{O}_5$  nanosheets.

#### Effect of scavenging agents on dye degradation

The MB dye contains active sites for oxidative attack. To understand the active oxidative species involved in the catalytic process, the effects of scavenging reagents in quenching superoxide ( $\text{O}_2^-$ ) and hydroxyl ( $\text{OH}$ ) radicals during the catalytic process were studied. *p*-Benoquinone and isopropanol were used as the scavenging reagents for superoxide ( $\text{O}_2^-$ ) and hydroxyl ( $\text{OH}$ ) radicals, respectively. *p*-benzoquinone and isopropanol were added at concentrations of 10 mM and 20 mM, respectively. The catalytic degradation of the MB dye molecule was studied

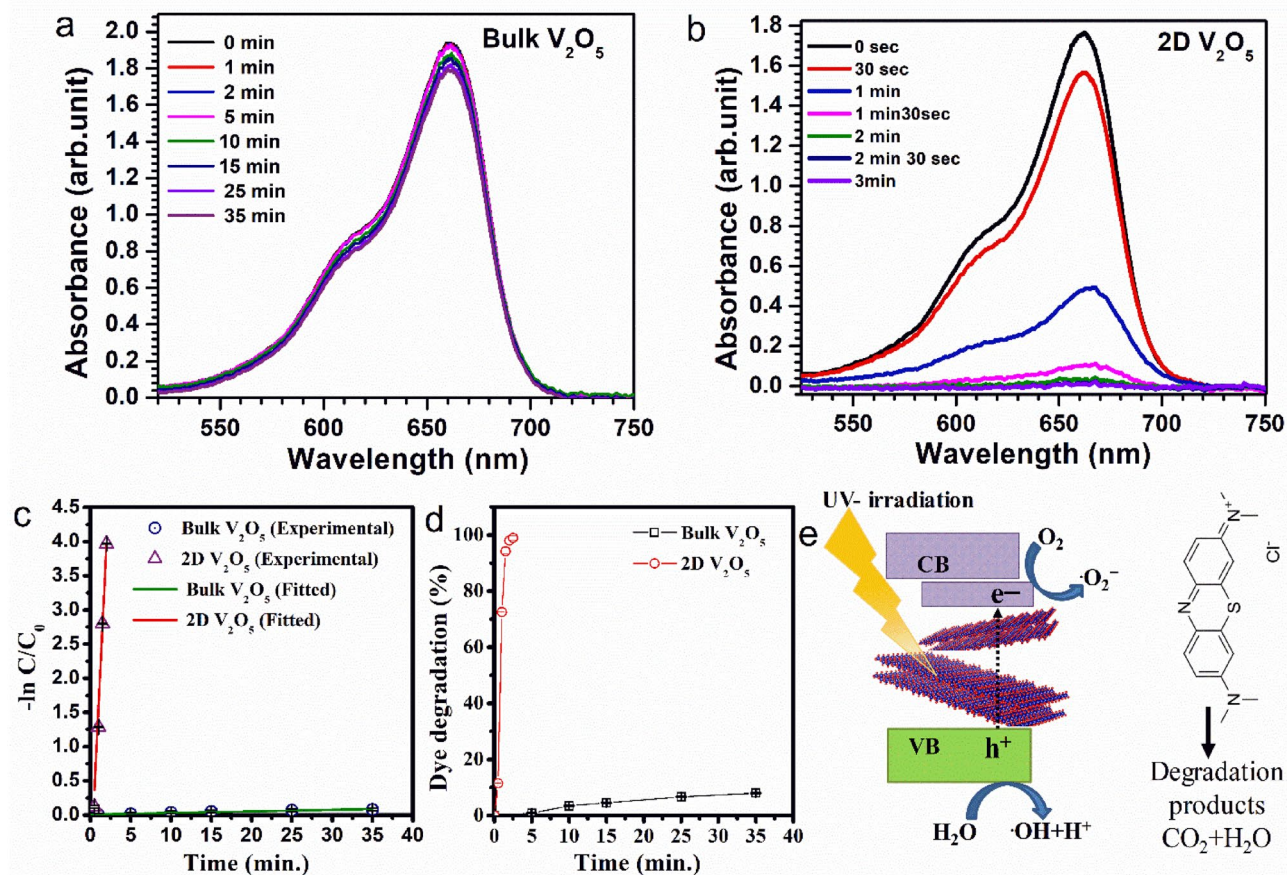
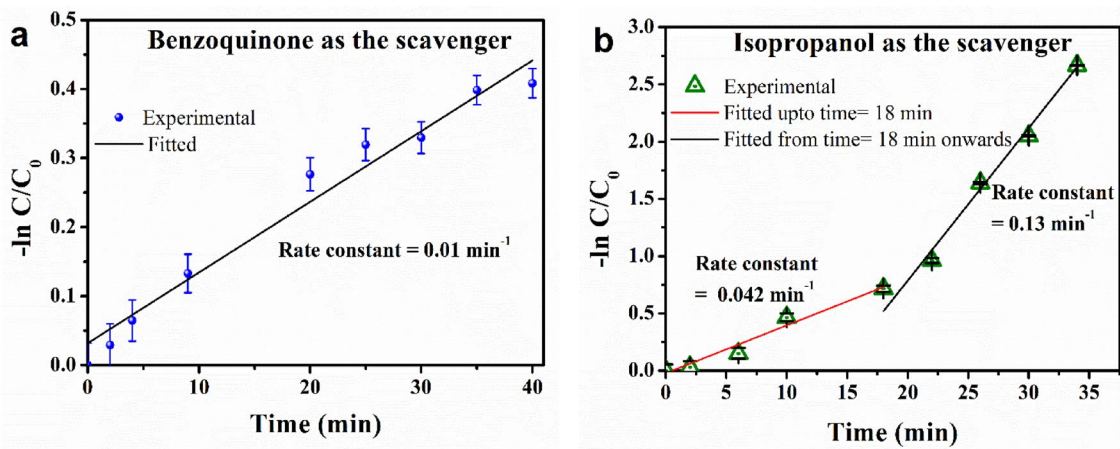


**Figure 3.** UV–Vis absorption spectra of MB dye solutions for different durations with (a) bulk  $\text{V}_2\text{O}_5$  and (b) 2D  $\text{V}_2\text{O}_5$  as catalysts. (c) The curve of  $-\ln (\text{C}_0/\text{C}_t)$  vs. light exposure time (d) Dye degradation efficiency using the bulk and 2D  $\text{V}_2\text{O}_5$  samples as catalysts versus the duration of light exposure. (e) Schematic of dye degradation mechanism of 2D  $\text{V}_2\text{O}_5$ .

Photocatalyst	Rate constant $\text{min}^{-1}$	Degradation time (min)	Efficiency (%)	Reference
$\text{V}_2\text{O}_5$ np	0.00742	20	31	<sup>44</sup>
rGO- $\text{V}_2\text{O}_5$	0.0184	20	71	<sup>44</sup>
rGO- $\text{V}_2\text{O}_5$	0.0078	255	85	<sup>45</sup>
$\text{V}_2\text{O}_5$ -nanorods	0.00135	300	24	<sup>46</sup>
$\text{V}_2\text{O}_5$ thin film	–	210	75	<sup>47</sup>
$\text{V}_2\text{O}_5$ np	0.025	–	92	<sup>48</sup>
Graphene- $\text{V}_2\text{O}_5$	0.0367	90	98	<sup>27</sup>
$\text{Nd}^{3+}$ doped $\text{V}_2\text{O}_5$	–	120	80	<sup>49</sup>
$\text{Ho}$ -doped $\text{V}_2\text{O}_5$	–	160	93	<sup>50</sup>
$\text{Yb}$ -doped $\text{V}_2\text{O}_5$	–	160	95	<sup>50</sup>
$\text{Na}_2\text{Ti}_3\text{O}_7/\text{V}_2\text{O}_5/g\text{-C}_3\text{N}_4$	0.103	–	–	<sup>51</sup>
$\text{Na}_2\text{Ti}_3\text{O}_7/\text{V}_2\text{O}_5$	0.0865	–	–	<sup>52</sup>
$\text{V}_2\text{O}_5$ /rGO	0.048	100	98	<sup>53</sup>
2D $\text{V}_2\text{O}_5$	2.311	3	~ 99	Present study

**Table 1.** Comparison of the present study on the photocatalytic degradation of MB dye using a 2D  $\text{V}_2\text{O}_5$  catalyst with the reported literature on related materials as catalysts.

using the same method as described in the previous sections. Figure S3a and b show the UV–Vis absorption spectra of MB dye molecules in the presence of the 2D  $\text{V}_2\text{O}_5$  catalyst and the scavengers *p*-benzoquinone and isopropanol, respectively. Figure 4a and b show the rate constants obtained in the presence of *p*-benzoquinone and isopropanol, respectively. The rate constant of the catalytic degradation of MB dye decreased to  $0.01 \text{ min}^{-1}$  in the presence of *p*-benzoquinone, while it decreased to  $2.31 \text{ min}^{-1}$  without any scavengers. In the presence



of isopropanol, the rate constant decreased to  $0.04 \text{ min}^{-1}$  during the first 18 min of UV light illumination, followed by a rate constant of  $0.13 \text{ min}^{-1}$ . This change in the rate constant is due to the decrease in the isopropanol concentration due to evaporation. In the presence of both scavenging reagents, a significant reduction in the rate constant is observed. The change in rate constant indisputably proves that the  $\cdot O_2$  and  $\cdot OH$  radicals are involved in the photocatalytic reaction.

#### Mechanism of photocatalytic degradation of MB dye

Figure 3e shows a schematic illustration of a possible pathway for the photocatalytic degradation of MB dye. When 2D  $V_2O_5$  nanosheets are exposed to UV light, electrons are excited to the conduction band (CB), leaving holes in the valence band (VB).  $\cdot OH$  radicals are generated when these holes interact with  $OH^-$  on the catalyst surface. These electrons lead to the production of  $O_2^-$  superoxide anion radicals. The effect of scavengers on dye degradation has demonstrated that the oxidizing species in the photocatalysis reaction are  $\cdot OH$  and  $\cdot O_2$  radicals that are thereby produced. According to the results, the use of 2D  $V_2O_5$  nanosheets effectively improved the separation of electrons and holes, which substantially enhanced the photocatalytic activity. The anticipated decrease in the screening effect of charges and the presence of excitonic levels in 2D materials could also be responsible for this enhanced separation of electrons and holes<sup>54</sup> in 2D  $V_2O_5$ .

#### Recyclability of the catalyst

The recyclability of the 2D  $V_2O_5$  catalyst was determined by reusing a 2D  $V_2O_5$  sample coated on a quartz substrate. After each cycle, the sample on the substrate was collected, washed with deionized water (Millipore), and dried at  $80^\circ\text{C}$ . Figure 5a shows the degradation efficiency of the catalyst under UV light illumination, and Fig. 5b shows the degradation efficiency of the 2D  $V_2O_5$  catalyst under UV light illumination for 3.5 min over three cycles. The decrease in efficiency can be due to the loss of catalyst from the substrate during the recycling process.

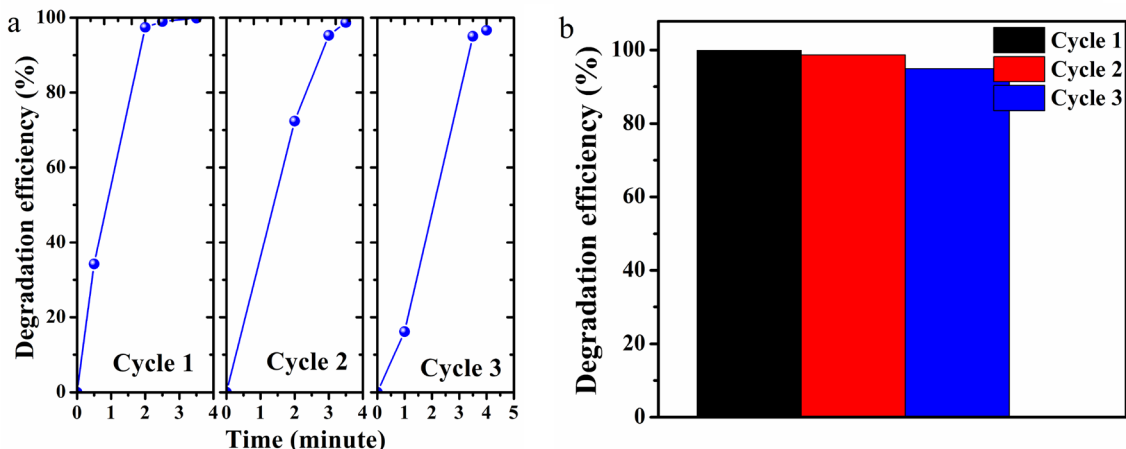


**Figure 5.** (a) MB dye degradation efficiency for three cycles of reuse of 2D  $V_2O_5$  nanosheets. (b) Bar diagram showing the dye degradation efficiency after 3.5 min of UV light exposure for three cycles.

## Conclusions

2D  $V_2O_5$  nanosheets with a bilayer thickness were synthesized using a chemical exfoliation technique, which showed a ~30-fold increase in the specific surface area from that of the bulk. The catalytic activity of 2D  $V_2O_5$  was studied in detail and compared with that of bulk  $V_2O_5$ . A considerable improvement in the degradation rate constant was observed for 2D  $V_2O_5$  from bulk  $V_2O_5$  catalysts. The rate constants for the bulk and 2D  $V_2O_5$  catalysts were 0.0023 and 2.311  $min^{-1}$ , respectively. The sizable improvement in the catalytic activity is attributed to three properties:

- A massive increase in the specific surface area of 2D nanosheets from bulk  $V_2O_5$  was observed as a result of the formation of nanosheets with thicknesses down to the bilayer.
- The presence of oxygen vacancies acts as an active site for redox reactions, improving the surface activity.
- An increase in the optical absorption coefficient on the order of ~7 times substantiates a significant increase in the number of photoexcited electrons. The efficient separation of photogenerated carriers facilitates the generation of free radicals responsible for the oxidative decomposition of organic dye molecules.

The results obtained from the present study undeniably prove that the novel 2D  $V_2O_5$  nanosheet is a promising photocatalyst. In addition, the 2D  $V_2O_5$  catalyst is stable and abundant on earth, the catalyst is recyclable, and the synthesis method of the catalyst is cost effective. Additionally, the current study opens up new possibilities for using 2D  $V_2O_5$  as electro- and photocatalyst because of its improved surface and optical properties. The increase in optical absorption leads to the possibility of efficiently generating hot electrons, creating novel possibilities for light energy conversion to electrical and chemical energy.

## Data availability

The datasets generated and analyzed during the current study are available from the corresponding author upon reasonable request.

Received: 16 November 2023; Accepted: 20 June 2024

Published online: 24 June 2024

## References

- Deng, D. *et al.* Catalysis with two-dimensional materials and their heterostructures. *Nat. Nanotechnol.* **11**, 218–230. <https://doi.org/10.1038/nnano.2015.340> (2016).
- Babar, Z. U., Raza, A., Cassinese, A. & Iannotti, V. Two dimensional heterostructures for optoelectronics: Current status and future perspective. *Molecules* **28**, 2275. <https://doi.org/10.3390/molecules28052275> (2023).
- Ali, S. *et al.* Recent advances in 2D-MXene based nanocomposites for optoelectronics. *Adv. Mater. Interfaces* **9**, 2200556. <https://doi.org/10.1002/admi.202200556> (2022).
- Raza, A. *et al.* Photoelectrochemical energy conversion over 2D materials. *Photochemistry* **2**, 272–298. <https://doi.org/10.3390/photochem2020020> (2022).
- Hassan, J. Z. *et al.* 2D material-based sensing devices: An update. *J. Mater. Chem. A* **11**, 6016–6063. <https://doi.org/10.1039/D2TA07653E> (2023).
- Raza, A., Qumar, U., Rafi, A. A. & Ikram, M. MXene-based nanocomposites for solar energy harvesting. *Sustain. Mater. Technol.* **33**, e00462. <https://doi.org/10.1016/j.susmat.2022.e00462> (2022).
- Raza, A., Rafi, A. A., Hassan, J. Z., Rafiq, A. & Li, G. Rational design of 2D heterostructured photo- & electrocatalysts for hydrogen evolution reaction: A review. *Appl. Surf. Sci. Adv.* **15**, 100402. <https://doi.org/10.1016/j.apsadv.2023.100402> (2023).
- Devarayapalli, K. C. *et al.* Mesostructured g-C<sub>3</sub>N<sub>4</sub> nanosheets interconnected with  $V_2O_5$  nanobelts as electrode for coin-cell-type-asymmetric supercapacitor device. *Mater. Today Energy* **21**, 100699. <https://doi.org/10.1016/j.mtener.2021.100699> (2021).
- Zhang, S. *et al.* Measuring the specific surface area of monolayer graphene oxide in water. *Mater. Lett.* **261**, 127098. <https://doi.org/10.1016/j.matlet.2019.127098> (2020).
- Wang, H. *et al.* 3D honeycomb-like structured graphene and its high efficiency as a counter-electrode catalyst for dye-sensitized solar cells. *Angew. Chem.* **52**, 9210–9214. <https://doi.org/10.1002/anie.201303497> (2013).
- Nakada, K. *et al.* Edge state in graphene ribbons: Nanometer size effect and edge shape dependence. *Phys. Rev. B* **54**, 17954–17961. <https://doi.org/10.1103/PhysRevB.54.17954> (1996).
- Zhao, L. *et al.* A critical review on new and efficient 2D materials for catalysis. *Adv. Mater. Interfaces* **9**, 2200771. <https://doi.org/10.1002/admi.202200771> (2022).
- Kumari, H. *et al.* A review on photocatalysis used for wastewater treatment: Dye degradation. *Water Air Soil Pollut.* **234**, 349. <https://doi.org/10.1007/s11270-023-06359-9> (2023).
- Javaid, R. *et al.* Catalytic oxidation process for the degradation of synthetic dyes: An overview. *Int. J. Environ. Res. Public Health* **16**, 2066. <https://doi.org/10.3390/ijerph16112066> (2019).
- Kapoor, R. T. *et al.* Exploiting microbial biomass in treating azo dyes contaminated wastewater: Mechanism of degradation and factors affecting microbial efficiency. *J. Water Process Eng.* **43**, 102255. <https://doi.org/10.1016/j.jwpe.2021.102255> (2021).
- Védrine, J. C. Metal oxides in heterogeneous oxidation catalysis: State of the art and challenges for a more sustainable world. *ChemSusChem* **12**, 577–588. <https://doi.org/10.1002/cssc.201802248> (2019).
- Beaula Ruby Kamalam, M. *et al.* Direct sunlight-driven enhanced photocatalytic performance of  $V_2O_5$  nanorods/graphene oxide nanocomposites for the degradation of Victoria blue dye. *Environ. Res.* **199**, 111369. <https://doi.org/10.1016/j.envres.2021.111369> (2021).
- Sahu, B. K. *et al.* Interface of GO with  $SnO_2$  quantum dots as an efficient visible-light photocatalyst. *Chemosphere* **276**, 130142. <https://doi.org/10.1016/j.chemosphere.2021.130142> (2021).
- Fu, M. *et al.* Sol-gel preparation and enhanced photocatalytic performance of Cu-doped ZnO nanoparticles. *Appl. Surf. Sci.* **258**, 1587–1591. <https://doi.org/10.1016/j.apsusc.2011.10.003> (2011).
- Agorka, E. S., Kuvarega, A. T., Mamba, B. B., Pandey, A. C. & Mishra, A. K. Enhanced visible-light photocatalytic activity of multielements-doped  $ZrO_2$  for degradation of indigo carmine. *J. Rare Earths* **33**, 498–506. [https://doi.org/10.1016/S1002-0721\(14\)60447-6](https://doi.org/10.1016/S1002-0721(14)60447-6) (2015).
- Hosseini, Z. S. *et al.* Enhanced visible photocatalytic performance of undoped  $TiO_2$  nanoparticles thin films through modifying the substrate surface roughness. *Mater. Chem. Phys.* **279**, 125530. <https://doi.org/10.1016/j.matchemphys.2021.125530> (2022).

22. Shi, Q., Zhang, X., Li, Z., Raza, A. & Li, G. Plasmonic Au Nanoparticle of a Au/TiO<sub>2</sub>–C<sub>3</sub>N<sub>4</sub> heterojunction boosts up photooxidation of benzyl alcohol using LED light. *ACS Appl. Mater. Interfaces* **15**, 30161–30169. <https://doi.org/10.1021/acsami.3c03451> (2023).
23. Bahlawane, N. *et al.* Vanadium oxide compounds: Structure, properties, and growth from the gas phase. *Chem. Vapor Deposit.* **20**, 299–311. <https://doi.org/10.1002/cvde.201400057> (2014).
24. Ek, M. *et al.* Visualizing atomic-scale redox dynamics in vanadium oxide-based catalysts. *Nat. Commun.* **8**, 305. <https://doi.org/10.1038/s41467-017-00385-y> (2017).
25. Haber, J. *et al.* The structure and redox properties of vanadium oxide surface compounds. *J. Catal.* **102**, 52–63. [https://doi.org/10.1016/0021-9517\(86\)90140-5](https://doi.org/10.1016/0021-9517(86)90140-5) (1986).
26. Alfaro Cruz, M. R. *et al.* Hierarchical V<sub>2</sub>O<sub>5</sub> thin films and its photocatalytic performance. *Mater. Lett.* **324**, 132751. <https://doi.org/10.1016/j.matlet.2022.132751> (2022).
27. Shanmugam, M. *et al.* Enhanced photocatalytic performance of the graphene–V<sub>2</sub>O<sub>5</sub> nanocomposite in the degradation of methylene blue dye under direct sunlight. *ACS Appl. Mater. Interfaces* **7**, 14905–14911. <https://doi.org/10.1021/acsami.5b02715> (2015).
28. Le, T. K. *et al.* Relation of photoluminescence and sunlight photocatalytic activities of pure V<sub>2</sub>O<sub>5</sub> nanohollows and V<sub>2</sub>O<sub>5</sub>/RGO nanocomposites. *Mater. Sci. Semicond. Process.* **100**, 159–166. <https://doi.org/10.1016/j.mssp.2019.04.047> (2019).
29. Radhakrishnan, R. P. *et al.* Electronic and vibrational decoupling in chemically exfoliated bilayer thin two-dimensional V<sub>2</sub>O<sub>5</sub>. *J. Phys. Chem. Lett.* **12**, 9821–9829. <https://doi.org/10.1021/acs.jpclett.1c02637> (2021).
30. Wachs, I. E. Catalysis science of supported vanadium oxide catalysts. *Dalton Trans.* **42**, 11762–11769. <https://doi.org/10.1039/C3DT50692D> (2013).
31. Rui, X. *et al.* Ultrathin V<sub>2</sub>O<sub>5</sub> nanosheet cathodes: Realizing ultrafast reversible lithium storage. *Nanoscale* **5**, 556–560. <https://doi.org/10.1039/C2NR33422D> (2013).
32. Reshma, P. R. 2D V<sub>2</sub>O<sub>5</sub> nanosheets for photocatalytic and advanced energy storage applications. *IGC News.* **133**, 4–8 (2022).
33. McCrory, C. C. L. *et al.* Benchmarking heterogeneous electrocatalysts for the oxygen evolution reaction. *J. Am. Chem. Soc.* **135**, 16977–16987. <https://doi.org/10.1021/ja407115p> (2013).
34. Meyer, J. C. *et al.* The structure of suspended graphene sheets. *Nature* **446**, 60–63. <https://doi.org/10.1038/nature05545> (2007).
35. Basu, R. *et al.* Role of vanadyl oxygen in understanding metallic behavior of V<sub>2</sub>O<sub>5</sub>(001) nanorods. *J. Phys. Chem. C* **120**, 26539–26543. <https://doi.org/10.1021/acs.jpcc.6b08452> (2016).
36. Wu, Q.-H. *et al.* Photoelectron spectroscopy study of oxygen vacancy on vanadium oxides surface. *Appl. Surf. Sci.* **236**, 473–478. <https://doi.org/10.1016/j.apsusc.2004.05.112> (2004).
37. Lambrecht, W. *et al.* On the origin of the split-off conduction bands in V<sub>2</sub>O<sub>5</sub>. *J. Phys. C* **32**, 4785. <https://doi.org/10.1088/0022-3719/14/32/015> (1981).
38. Mak, K. F. *et al.* Tightly bound trions in monolayer MoS<sub>2</sub>. *Nat. Mater.* **12**, 207–211. <https://doi.org/10.1038/nmat3505> (2013).
39. Madapu, K. K. & Dhara, S. Laser-induced anharmonicity vs thermally induced biaxial compressive strain in mono- and bilayer MoS<sub>2</sub> grown via CVD. *AIP Adv.* **10**, 085003. <https://doi.org/10.1063/5.0001863> (2020).
40. Trasatti, S. *et al.* Real surface area measurements in electrochemistry. *AIP Adv.* **63**, 711–734. <https://doi.org/10.1351/pac199163050711> (1991).
41. Liu, X. *et al.* Visible light photocatalytic degradation of methylene blue by SnO<sub>2</sub> quantum dots prepared via microwave-assisted method. *Catal. Sci. Technol.* **3**, 1805–1809. <https://doi.org/10.1039/C3CY00013C> (2013).
42. Chen, F. *et al.* A facile route for the synthesis of ZnS rods with excellent photocatalytic activity. *Chem. Eng. J.* **234**, 223–231. <https://doi.org/10.1016/j.cej.2013.08.075> (2013).
43. Jin, X. *et al.* Influences of synthetic conditions on the photocatalytic performance of ZnS/graphene composites. *J. Alloys Compd.* **780**, 299–305. <https://doi.org/10.1016/j.jallcom.2018.11.271> (2019).
44. Mishra, A. *et al.* Rapid photodegradation of methylene blue dye by rGO–V<sub>2</sub>O<sub>5</sub> nano composite. *J. Alloys Compd.* **842**, 155746. <https://doi.org/10.1016/j.jallcom.2020.155746> (2020).
45. Awani, E. *et al.* Synthesis and characterization of reduced graphene oxide–V<sub>2</sub>O<sub>5</sub> nanocomposite for enhanced photocatalytic activity under different types of irradiation. *J. Phys. Chem. Solids* **125**, 8–15. <https://doi.org/10.1016/j.jpcs.2018.09.028> (2019).
46. Jayaraj, S. K. *et al.* Enhanced photocatalytic activity of V<sub>2</sub>O<sub>5</sub> nanorods for the photodegradation of organic dyes: A detailed understanding of the mechanism and their antibacterial activity. *Mater. Sci. Semicond. Process.* **85**, 122–133. <https://doi.org/10.1016/j.mssp.2018.06.006> (2018).
47. Liu, H. *et al.* Growth of oriented vanadium pentaoxide nanostructures on transparent conducting substrates and their applications in photocatalysis. *J. Solid State Chem.* **214**, 79–85. <https://doi.org/10.1016/j.jssc.2013.10.020> (2014).
48. Jenifer, A. *et al.* Photocatalytic dye degradation of V<sub>2</sub>O<sub>5</sub> nanoparticles: An experimental and DFT analysis. *Optik* **243**, 167148. <https://doi.org/10.1016/j.ijleo.2021.167148> (2021).
49. Fauzi, M. *et al.* The effect of various capping agents on V<sub>2</sub>O<sub>5</sub> morphology and photocatalytic degradation of dye. *J. Mater. Sci. Mater. Electron.* **32**, 10473–10490. <https://doi.org/10.1007/s10854-021-05703-1> (2021).
50. Yadav, A. A., Hunge, Y. M., Kang, S.-W., Fujishima, A. & Terashima, C. Enhanced photocatalytic degradation activity using the V<sub>2</sub>O<sub>5</sub>/RGO composite. *Nanomaterials* <https://doi.org/10.3390/nano13020338> (2023).
51. Vattikuti, S. V. P., Nam, N. D. & Shim, J. Graphitic carbon nitride/Na<sub>2</sub>Ti<sub>3</sub>O<sub>7</sub>/V<sub>2</sub>O<sub>5</sub> nanocomposite as a visible light active photocatalyst. *Ceram. Int.* **46**, 18287–18296. <https://doi.org/10.1016/j.ceramint.2020.05.045> (2020).
52. Vattikuti, S. V. P., Reddy, P. A. K., NagaJyothi, P. C., Shim, J. & Byon, C. Hydrothermally synthesized N<sub>a</sub>2Ti<sub>3</sub>O<sub>7</sub> nanotube–V<sub>2</sub>O<sub>5</sub> heterostructures with improved visible photocatalytic degradation and hydrogen evolution: Its photocorrosion suppression. *J. Alloys Compd.* **740**, 574–586. <https://doi.org/10.1016/j.jallcom.2017.12.371> (2018).
53. Kabir, M. H. *et al.* The efficacy of rare-earth doped V<sub>2</sub>O<sub>5</sub> photocatalyst for removal of pollutants from industrial wastewater. *Opt. Mater.* **147**, 114724. <https://doi.org/10.1016/j.optmat.2023.114724> (2024).
54. Zhang, D. *et al.* Tailoring of electronic and surface structures boosts exciton-triggering photocatalysis for singlet oxygen generation. *Proc. Natl. Acad. Sci. USA* **118**, e2114729118. <https://doi.org/10.1073/pnas.2114729118> (2021).

## Acknowledgements

The authors thank Dr. K Ganesan for the AFM studies and Dr. Shyam Kanta Sinha and Dr. Arup Das Gupta for the TEM studies. The authors also thank Dr. A. Das and Ms. Reshma T S for fruitful discussions. We also acknowledge the Director, MSG, and the Director, IGCAR, for their encouragement.

## Author contributions

The central idea was conceived by R.P.R. and A.K.P. Sample synthesis, characterization, and data analysis were carried out by R.P.R. The manuscript was written by R.P.R., and all the authors discussed the results and the manuscript.

## Competing interests

The authors declare no competing interests.

### Additional information

**Supplementary Information** The online version contains supplementary material available at <https://doi.org/10.1038/s41598-024-65421-6>.

**Correspondence** and requests for materials should be addressed to P.R.R. or A.K.P.

**Reprints and permissions information** is available at [www.nature.com/reprints](http://www.nature.com/reprints).

**Publisher's note** Springer Nature remains neutral with regard to jurisdictional claims in published maps and institutional affiliations.



**Open Access** This article is licensed under a Creative Commons Attribution 4.0 International License, which permits use, sharing, adaptation, distribution and reproduction in any medium or format, as long as you give appropriate credit to the original author(s) and the source, provide a link to the Creative Commons licence, and indicate if changes were made. The images or other third party material in this article are included in the article's Creative Commons licence, unless indicated otherwise in a credit line to the material. If material is not included in the article's Creative Commons licence and your intended use is not permitted by statutory regulation or exceeds the permitted use, you will need to obtain permission directly from the copyright holder. To view a copy of this licence, visit <http://creativecommons.org/licenses/by/4.0/>.

© The Author(s) 2024